

# Cobalt–Copper-Embedded Nitrogen-Doped Carbon Nanostructures Derived from Zeolite Imidazolate Frameworks as Electrocatalysts for the Oxygen Reduction Reaction

Sunguk Noh, Hyejin Oh, Jihyun Kim, Sojin Jung, and Jun Ho Shim\*

Cite This: *ACS Omega* 2024, 9, 29431–29441

Read Online

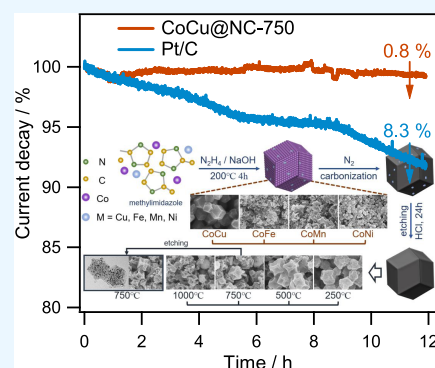
ACCESS |

Metrics &amp; More

Article Recommendations

Supporting Information

**ABSTRACT:** In recent years, researchers have focused on developing zeolite imidazolate frameworks (ZIFs) as an alternative to Pt electrocatalysts for various applications, including water splitting, lithium–air batteries, zinc-air batteries, and fuel cells. In this study, we synthesized CoCu-ZIF to be used as a precursor in the development of cathode catalysts for the oxygen reduction reaction (ORR) in fuel cells. Hydrazine played a crucial role in maintaining uniformity in the development and particle size of the ZIF-67 structures. Moreover, it facilitated the rapid formation of the ZIF-67 structures at higher temperatures. A unique pseudorhombic dodecahedral morphology was obtained at a Co/Cu molar ratio of 7:3. Among all the synthesized N-doped carbon nanostructures embedded with Co and Cu nanoparticles, CoCu@NC-750, pyrolyzed at 750 °C, showed superior ORR catalytic performance. This catalyst exhibited a notably higher half-wave potential of 0.816 V and demonstrated a clear 4-electron transfer mechanism. The overpotential of CoCu@NC-750 shifted by only 11 mV over 10,000 cyclic voltammetry cycles, whereas a 55 mV shift was observed for Pt/C. CoCu@NC-750 exhibited a ~0.8% decrease in current density during a 12-h ORR, in contrast to the 8.3% decline shown by Pt/C. This superior catalytic activity and stability can be attributed to factors such as higher oxygen adsorption induced by the N-doped carbon layer due to the localized changes in electron density and the enhanced stability of the bimetallic core. Our findings suggest that CoCu@NC-750 is a promising alternative to Pt/C in fuel cell cathodes.



## INTRODUCTION

The demand for sustainable energy solutions continues to increase with increasing fossil fuel consumption.<sup>1,2</sup> Therefore, advanced research on energy generation and utilization technologies is crucial for a safe and sustainable future.<sup>3–5</sup> The electrocatalytic oxygen reduction reaction (ORR) is essential for energy conversion and storage in devices such as fuel cells and metal-air batteries.<sup>5–16</sup> Despite the widespread use of Pt-based catalysts, their high cost, limited durability, and low methanol tolerance require the development of optimal materials for ORR catalysts.<sup>15–17</sup> Hence, researchers have focused on the development of carbon-based ORR catalysts with high ORR catalytic activity as alternatives to Pt. Nanostructures based on graphene<sup>18</sup> or oxidized graphene<sup>19</sup> and carbon-based catalysts doped with heteroatoms<sup>20</sup> are at the forefront of this research effort. When combined with transition-metal catalysts, these carbon structures display synergistic effects in ORR catalysis.<sup>21–23</sup> Furthermore, the substantial presence of graphite carbon in carbon-based ORR catalysts boosts conductivity, enabling faster electron transfer and enhanced ORR activity.<sup>17,24</sup> In particular, high porosity and large surface area are essential structural features for an ideal carbon-based ORR catalyst, which enable rapid material transport and easy access to ORR active sites.

Among the various methods, fabricating carbon-based ORR catalysts from metal–organic framework (MOF) materials is considered an excellent strategy because the diverse composition and structural variability of MOFs can generate ideal ORR catalysts.<sup>25–27</sup> In particular, zeolitic imidazolate framework (ZIF) materials are among the most promising precursor materials as they contain sufficient nitrogen atoms within their porous structures.<sup>27–29</sup> To date, various carbon-based ORR catalysts have been manufactured using different types of ZIF materials. Among them, ZIF-67, consisting of the commonly used ligand 2-methylimidazole and metal ions, has attracted significant attention.<sup>30</sup> The exceptional flexibility in engineering the structure, morphology, and composition of ZIF-67 and its derivatives facilitated their applications in secondary batteries,<sup>31</sup> supercapacitors,<sup>32</sup> fuel cells,<sup>33</sup> gas adsorption and separation,<sup>34</sup> and electrochemical and photoelectrochemical water electrolysis.<sup>35</sup> Nevertheless, most ZIFs

Received: February 21, 2024

Revised: May 10, 2024

Accepted: June 14, 2024

Published: June 26, 2024



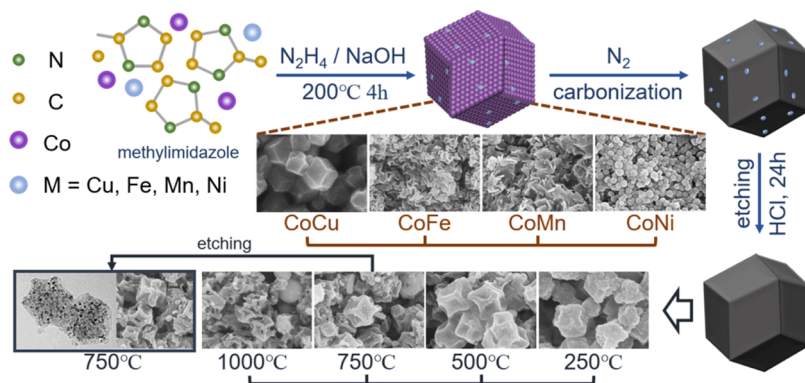


**Figure 1.** Schematic of the synthesis of CoCu@NC for applications in the electrochemical ORR.

exhibit poor electrical conductivity, which hinders their application in electrocatalysis.<sup>30,36</sup> Moreover, certain ZIFs can lose structural stability during pyrolysis, which complicates the optimization of their inherent catalytic activity.<sup>30,36</sup>

Compared to single-metal ZIF structures, bimetallic catalysts exhibit enhanced catalytic activity and stability upon modulating the electronic structures of their metals, which induce synergistic effects on their catalytic activities. According to theoretical calculations, Cu displays the highest ORR activity among nonprecious transition metals due to its proximity to Pt at the peak of the “volcano plot”.<sup>37</sup> However, Cu-based carbon materials obtained through pyrolysis encounter issues such as self-aggregation, irreversible integration, and surface oxidation, each of which is detrimental to their electrocatalytic performance due to the large diffusion coefficient of Cu ions.<sup>38</sup> When the content of Cu ions in a ZIF matrix reaches a certain limit, they cannot be completely stabilized by N-doped sites and are partially reduced to metallic Cu atoms, subsequently aggregating into nanoparticles during pyrolysis.<sup>27,39,40</sup> Therefore, a bimetallic mixture at the optimal precursor concentration in the ZIF structure can potentially exhibit synergistic effects on catalytic activity and stability upon tuning its properties.

In this study, we employed a polyol method using hydrazine to accelerate the synthesis of a stable ZIF structure. Uniformly sized pseudorhombic dodecahedral cages were obtained in the CoCu(7:3)-ZIF structure from various bimetal combinations in CoM-ZIF (where M = Fe, Mn, and Ni). The CoCu-embedded N-doped carbon nanostructure (CoCu@NC), which maintains the structural form of CoCu(7:3)-ZIF, was produced through high-temperature pyrolysis at 750 °C. Subsequently, we evaluated the electrochemical catalytic activity by conducting experiments to compare the performances of single-metal-incorporated structures, specifically Co@NC-750 and Cu@NC-750, with various bimetal combinations of CoM@NC (M = Fe, Mn, and Ni). The resulting CoCu@NC-750 exhibited superior ORR catalytic activity in an alkaline solution compared to the other prepared catalysts and was comparable to that of commercial Pt/C. Therefore, CoCu@NC-750 is a promising replacement for Pt/C in fuel cell cathodes.

## EXPERIMENTAL SECTION

**Materials and reagents.** Cobalt chloride hexahydrate ( $\text{CoCl}_2 \cdot 6\text{H}_2\text{O}$ ), ethylene glycol, NaOH, and HCl were purchased from Duksan (reagent grade, South Korea). Copper(II) chloride dihydrate ( $\text{CuCl}_2 \cdot 2\text{H}_2\text{O}$ ), 2-methylimida-

zole, and poly(vinylpyrrolidone) (PVP) were purchased from Sigma-Aldrich (analytical grade). Hydrazine monohydrate ( $\text{N}_2\text{H}_4$ ; 79%) was obtained from TCI (technical grade, Japan). The carbon support (Vulcan XC-72) and the commercial 20 wt % Pt/C catalyst were both procured from Premetek. All solutions for this study were prepared using purified water (Milli-Q, 18 M $\Omega$ -cm).

**Physicochemical Characterization.** The surface and morphological properties of the synthesized catalysts were comprehensively characterized using a suite of analytical techniques. Field emission scanning electron microscopy (FESEM, Hitachi S-4800) equipped with an energy-dispersive X-ray spectroscopy (EDS) attachment and high-resolution transmission electron microscopy (HR-TEM, Hitachi HF-3300, and Titan G2) were employed to investigate the catalysts’ microscopic features. Additionally, high-angle annular dark-field scanning transmission electron microscopy (HAADF-STEM, Titan G2 ChemiSTEM Cs probe) provided detailed morphological insights. The structural properties and crystalline phases of the catalysts were determined using powder X-ray diffraction (XRD, Diatome MPD) with a standard Cu anode and  $K\alpha$  radiation ( $\lambda = 1.54 \text{ \AA}$ ). Chemical compositions and surface characteristics were analyzed through X-ray photoelectron spectroscopy (XPS, Thermo Scientific K-Alpha) utilizing a monochromatic Al  $K\alpha$  source. To assess the surface areas and pore-size distributions of the catalysts, Brunauer–Emmett–Teller (BET) analysis was conducted using a BELSORP-mini II instrument (Microtrac-BEL). Additional spectroscopic investigations included ultraviolet–visible (UV–vis) spectroscopy, performed with a Shimadzu UV-1900i spectrophotometer, Raman spectroscopy, utilizing an XploRA micro-Raman spectrophotometer with a 532 nm laser, and Fourier-transform infrared (FTIR) spectroscopy, recorded on a Thermo Fisher Scientific Nicolet iS5 FTIR spectrometer. These comprehensive analyses provided a thorough understanding of the physicochemical properties of the synthesized catalysts.

**Synthesis of CoCu-ZIF Nanocrystals.** The electrode catalyst for the fuel cell cathode was prepared using a ZIF structure, as shown in Figure 1. The reflux apparatus was connected to a three-neck round-bottom flask, and 100 mL of ethylene glycol (EG) was added.  $\text{CoCl}_2 \cdot 6\text{H}_2\text{O}$  (37.5 mM),  $\text{CuCl}_2 \cdot 2\text{H}_2\text{O}$  (12.5 mM), and PVP (1.67 g) were added to the flask. Subsequently, 5 mL of  $\text{N}_2\text{H}_4$  and 4.105 g of 2-methylimidazole were sequentially added to the solution. To adjust the pH, 5 mL of 5 M NaOH was carefully added to the mixture while stirring at room temperature. After 5 min, the

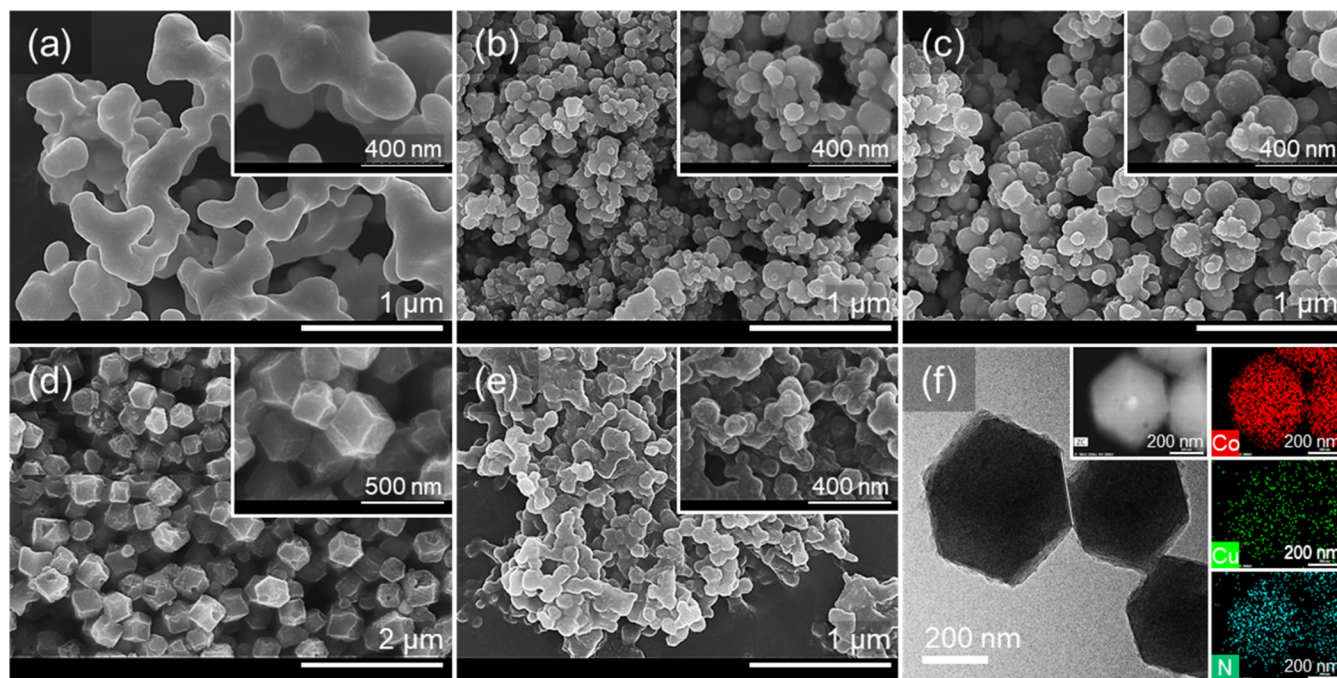


**Figure 2.** SEM images of CoCu-ZIF structures with different Co:Cu molar ratios in the presence of hydrazine: (a) CoCu-ZIF(10:0), (b) CoCu-ZIF(3:7), (c) CoCu-ZIF(5:5), (d) CoCu-ZIF(7:3), and (e) CoCu-ZIF(0:10). Insets (a–e): Enlarged images of each specimen. (f) TEM and TEM-EDS mapping images of CoCu-ZIF(7:3).

solution was slowly heated to the boiling point and maintained at that temperature for 4 h. After the reaction, the mixture was thoroughly washed with ethanol and distilled water and then freeze-dried. The following CoCu-ZIF samples with varying Co/Cu molar ratios were prepared: CoCu(10:0)-ZIF, CoCu(7:3)-ZIF, CoCu(5:5)-ZIF, CoCu(3:7)-ZIF, and CoCu(0:10)-ZIF. To compare the catalytic activities of the different types of metals, metal precursors of Fe, Mn, and Ni were synthesized under the same conditions and denoted as CoM-ZIF (M = Fe, Mn, and Ni). The Co/Cu ratio that exhibited the highest catalytic activity, i.e., CoCu(7:3)-ZIF, was adopted for the Co:M molar ratio. Each dried sample was stored in a sealed container until further use.

**Preparation of CoCu@NC.** Solid CoCu-ZIF (1.0 g) was subjected to pyrolysis for 2 h in a tube furnace with flowing  $N_2$ . The furnace temperature was gradually increased to 250, 500, 750, and 1000 °C at a rate of 5 °C per min to obtain the optimal fuel cell cathode sample. The resulting CoCu coated with the N-doped graphitized structures was named CoCu@NC-*t* (where *t* represents the pyrolysis temperature). The residual substances remaining on the surface of the ZIF structure after carbonization were removed by stirring in 12 M HCl for 24 h. Finally, the obtained CoCu@NC was sequentially washed with ethanol and distilled water and then freeze-dried. The CoM@NC samples (M = Fe, Mn, or Ni) were pyrolyzed under the same optimized conditions used for the pyrolysis of CoCu@NC.

**Electrochemical Characterization.** All electrochemical experiments were conducted using a three-electrode system, as in previous studies.<sup>41</sup> A rotating disk electrode (RDE) with an area of 0.071 cm<sup>2</sup> and a rotating-ring disk electrode (RRDE) with a disk area of 0.1256 cm<sup>2</sup> (disk) were used as the working electrode. A Hg/HgO electrode served as the reference electrode, and a Pt wire was used as the counter electrode. The working electrode was polished with alumina powder and

rinsed with distilled water via sonication to remove any remaining alumina powder. Each catalyst sample was dispersed in distilled water to obtain a concentration of 2.0 mg mL<sup>-1</sup>, and then 5 μL of the dispersed solution was introduced onto the working electrode three times (total volume = 15 μL) and dried in a vacuum desiccator. To prevent sample detachment, 5 μL of Nafion (0.05 wt %) was drop-coated onto the electrode surface. All electrochemical measurements for the ORR were performed in a 0.1 M KOH electrolyte with O<sub>2</sub> or N<sub>2</sub> purging. The measured potentials were converted to the reversible hydrogen electrode (RHE) scale using the equation  $E_{RHE} = E_{Hg/HgO} + (0.05916 \times pH) + 0.14$ . RRDE and cyclic voltammetry (CV) experiments were conducted using a CH instrument (CHI705E), and all electrochemical data were obtained within an appropriate potential range.

## RESULTS AND DISCUSSION

**Role of Hydrazine in Uniform ZIF Structure Formation.** Hydrazine (Hz) played a crucial role in polyol synthesis, facilitating the formation of uniform shapes in the ZIF-67 structures by regulating the reaction. CoCu-ZIF(7:3) produced without Hz (Figure S1) exhibited irregular particle sizes and agglomeration, resembling those of CoCu-ZIF(10:0) and/or CoCu-ZIF(0:10) (Figure 2a,e). This suggests that Hz is indispensable for achieving uniform shapes in ZIF structures under rapid synthesis conditions (≤4 h). Hence, CoCu-ZIF(7:3) prepared using Hz was used for the subsequent evaluation of electrocatalytic activities. Figure S2 shows the changes in color during the preparation of CoCu-ZIF(7:3) using Hz. Hz complexes with either Co<sup>2+</sup> or Cu<sup>2+</sup> in the presence of 2-methylimidazole (HMIM). During the reaction of  $Co^{2+} + 3N_2H_4 \rightarrow [Co(N_2H_4)_3]^{2+}$ ,<sup>42</sup> the color of the Co<sup>2+</sup> solution shifts from transparent magenta to magenta tinged with gray. However, the introduction of HMIM into the solution turns into a vivid purple shade owing to the formation

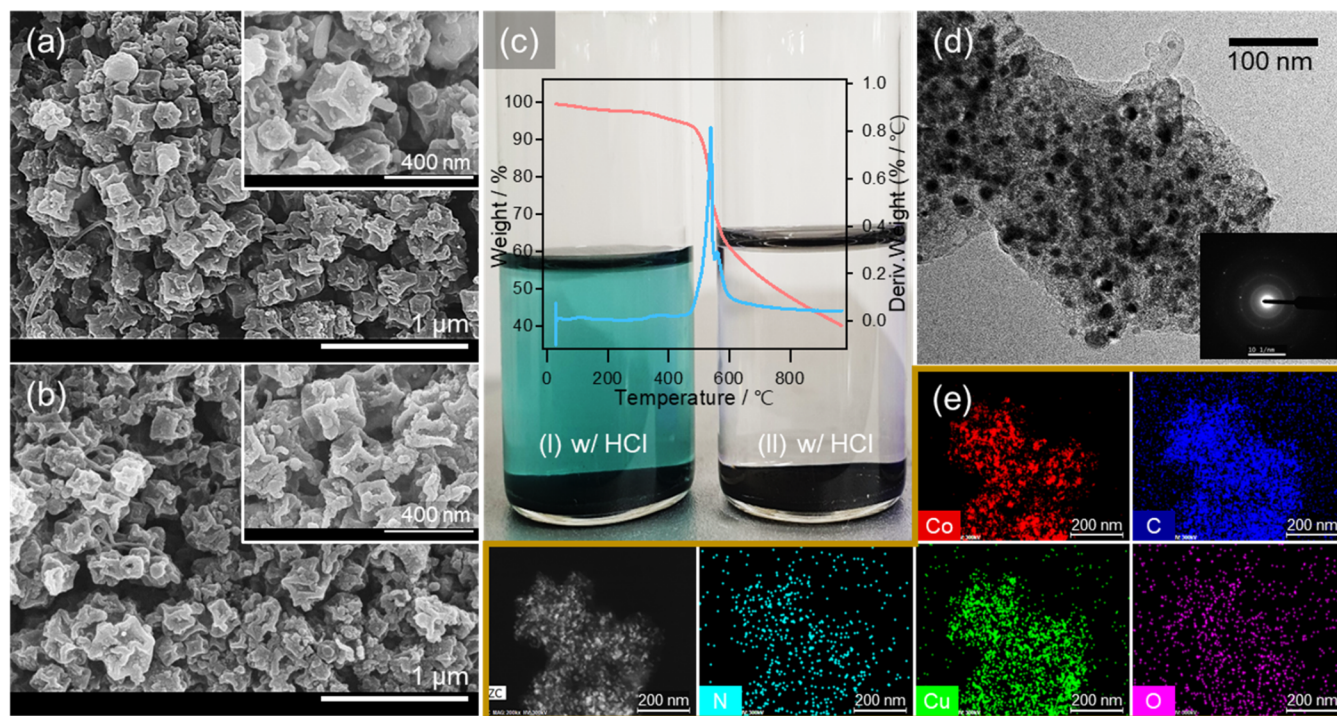


**Figure 3.** SEM images of CoCu@NC-750 (a) before and (b) after acid treatment. (c) TGA and photographs of the CoCu@NC-750 catalyst during treatment (left vial (I), dark cyan) and after treatment (right vial (II), transparent) in a HCl solution. (d) TEM (inset: corresponding SAED pattern) and (e) TEM-EDS elemental mapping images of CoCu@NC-750.

of a  $\text{Co}^{2+}$ -HMIM complex prompted by the pH elevation and finally turns into a deep purple color after the formation of the ZIF-67 structure. Gradual pH reduction via the addition of HCl leads to the protonation of HMIM, resulting in the decomplexation of  $\text{Co}^{2+}$ -HMIM to  $\text{Co}^{2+}$ -Hz, which transforms into the magenta-colored initial  $\text{Co}^{2+}$  solution. In contrast, no additional color changes were observed for the  $\text{Cu}^{2+}$  solution after turning brown upon the addition of Hz and/or HMIM, as the addition of HCl results in the formation of a colorless complex  $(\text{CuCl}_4)^{2-}$ . These chromatic transitions indicate the crucial role of Hz in facilitating the rapid formation of uniform ZIF structures via complexation with metal ions.

**Structural and Morphological Characteristics of CoCu-ZIF Precursors.** The structural and morphological characteristics of ZIF structures prepared using Hz and HMIM and different metal ion concentrations were investigated via SEM and TEM. The catalysts were labeled CoCu( $x$ : $y$ )-ZIF, where  $x$  and  $y$  represent the molar concentration ratios of  $\text{Co}^{2+}$  and  $\text{Cu}^{2+}$ . CoCu(10:0)-ZIF and CoCu(0:10)-ZIF were also synthesized using the same methodology. Despite minor differences in grain size between CoCu(10:0)-ZIF and CoCu(0:10)-ZIF, their morphologies closely resemble those of porous gold nanostructures produced by the dealloying method.<sup>43</sup> When an equal concentration of HMIM was used with an increasing Co:Cu molar ratio, the size of individual particles increased in the order of CoCu(3:7)-ZIF < CoCu(5:5)-ZIF < CoCu(7:3)-ZIF (Figure 2). Notably, CoCu(7:3)-ZIF exhibited a well-defined structure resembling a pseudorhombic dodecahedron cage, which is a representative ZIF structure (Figure 2d).

The TEM and EDS elemental mapping of CoCu(7:3)-ZIF (Figure 2f) demonstrated a uniform distribution of Co and Cu within each particle, which is consistent with the structure observed in the SEM results. Elemental mapping revealed a

higher density of Co than that of Cu, confirming the characteristic features of a typical ZIF-67.<sup>30,32–36</sup> Therefore, unless otherwise stated, the optimized CoCu(7:3)-ZIF was employed as the precursor for the fuel cell cathode catalyst. To compare the changes in the catalytic activities resulting from variations in transition-metal composition, CoM-ZIF (M = Fe, Mn, and Ni) catalysts were synthesized under the optimized conditions used for the preparation of CoCu-ZIF(7:3). Figure S3 shows the SEM images of CoFe-ZIF, CoMn-ZIF, and CoNi-ZIF. Unlike CoCu-ZIF, CoFe-ZIF and CoMn-ZIF formed plate-like structures with particle aggregation, whereas CoNi-ZIF exhibited spherical nanoparticles with diameters of approximately 90–100 nm.

**Structural Stability of CoCu@NC Catalysts.** To optimize the catalytic activity and stability of CoCu-ZIF, we observed the thermal decomposition behavior of CoCu-ZIF(7:3) at 250, 500, 750, and 1000 °C (Figures 3 and S4). The resulting N-doped graphitized structures were named CoCu@NC- $t$  (where  $t$  represents the pyrolysis temperature). The SEM images of CoCu@NC-750 show that the structural framework of CoCu-ZIF was maintained, even after acid treatment (Figure 3a,b). During pyrolysis, Co and Cu were vaporized, thus etching the carbon frameworks and creating additional voids inside the ZIFs. The residual nanoparticles and impurities adhering to the surface of CoCu@NC-750, which are associated with thermal decomposition, were easily removed by acid treatment. The photographs in Figure 3c show the as-synthesized CoCu@NC-750 catalyst immersed in an HCl solution. The dissolution of  $\text{Cu}^{2+}$  and  $[\text{Co}(\text{Cl})_4]^{2-}$  species during acid treatment (left vial) resulted in a dark cyan solution. No further metal leaching occurred upon completion of the acid treatment (right vial), which resulted in a transparent solution. The weight loss during the acid treatment

process was  $\leq 3\%$ , which confirmed the formation of a limited number of metal nanoparticles on the carbon surface.

The TGA analysis of the ZIF structure demonstrated minimal weight loss below 550 °C, indicating the preservation of structural stability (Figure 3c). This result is consistent with the reported thermal stability of ZIFs.<sup>44,45</sup> A sharp weight loss of more than 60% was observed as the temperature increased from 550 to 1000 °C, which indicated the thermal decomposition of the ZIF structure. Therefore, the pyrolysis temperatures of CoCu@NC-250 and CoCu@NC-500 were insufficient to trigger carbonization (Figure S4). During the thermal decomposition process, the external surface of the CoCu metal catalyst was transformed into a carbon structure doped with nitrogen atoms. The high temperature of over 800 °C caused the collapse of the ZIF framework (Figure S4), while the other samples retained their distinctive pseudorhombic dodecahedral framework. Hence, the most promising catalytic activity was expected from CoCu@NC-750, which retained the CoCu-ZIF scaffold while benefiting from carbonization. CoCu@NC-750 will be referred to as CoCu@NC if no temperature conditions are specified.

The TEM and STEM mapping images in Figure 3d,e, respectively, reveal the presence of both Co and Cu nanoparticles in CoCu@NC-750. The TEM images show that the metal–carbon boundary is encapsulated in carbon (Figures 3d and 4). The selected area electron diffraction

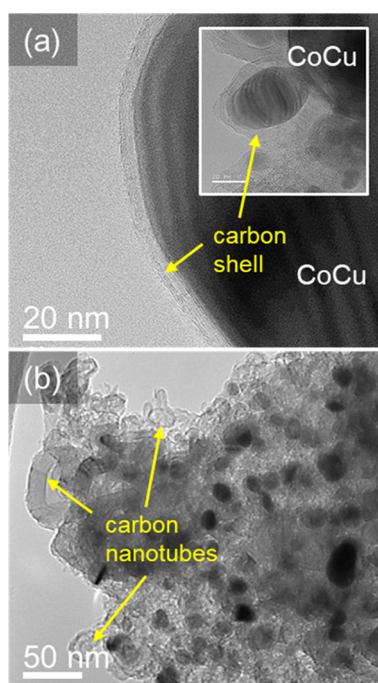


**Figure 4.** (a) HR-TEM and (b) TEM images of CoCu@NC-750.

(SAED) spot (inset of Figure 3d) indicates the partial crystallinity of the CoCu nanoparticles covered with the outer carbon layer. The Co nanoparticles exhibited a darker and larger appearance than the Cu nanoparticles and were distributed over a wide range within the carbon matrix. STEM elemental mapping provided evidence of a metal nanoparticle core surrounded by a carbon shell. The high-resolution TEM images shown in Figure 4a reveal metal nanoparticles encapsulated in carbon, which presumably helped prevent metal dissolution and enhanced the stability of the catalyst.

Furthermore, carbon nanotubes (CNTs) were partially observed in the outer region of the carbon layer (Figure 4b). This phenomenon can be attributed to the presence of a small number of vacant *d*-orbitals in the transition metal, which possess a strong affinity for carbon, forming weak bonds with the *p*-orbitals of carbon and leading to the generation of nanotubes.<sup>46,47</sup>

**Characterization of CoCu@NC Catalysts.** As shown in Figure 5a, the XRD pattern was used to analyze the chemical

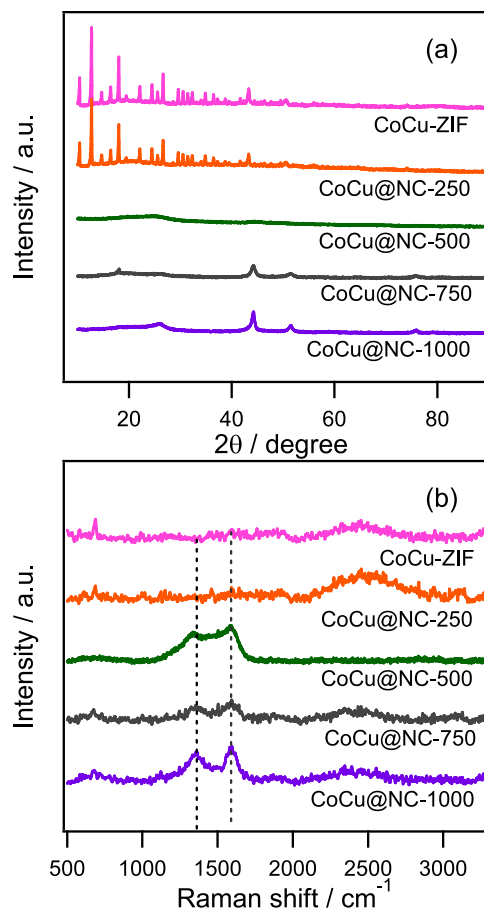


**Figure 5.** (a) XRD patterns and (b) Raman spectra of CoCu-ZIF, CoCu@NC-250, CoCu@NC-500, CoCu@NC-750, and CoCu@NC-1000.

structure and crystalline phase of the prepared sample. The XRD pattern of CoCu-ZIF is consistent with previously reported patterns.<sup>48</sup> The CoCu@NC-250 showed a lower peak intensity than that of CoCu-ZIF but maintained the same XRD pattern. However, CoCu@NC-500 did not exhibit a diffraction pattern or crystallinity, which indicates that 500 °C is insufficient for the pyrolysis of CoCu-ZIF. In contrast, CoCu@NC-750 and CoCu@NC-1000 exhibited diffraction peaks at  $2\theta = 44.1$  and  $51.4^\circ$ , corresponding to the (111) and (200) crystal planes of Co metals, respectively. Moreover, the diffraction pattern of CoCu@NC-750 corresponds to the fcc phase.<sup>49</sup> Notably, the overlap in the diffraction pattern of CoCu@NC could be attributed to the similarity in diffraction angles of Co and Cu.<sup>49</sup> The higher peak intensity of CoCu@NC-1000 than that of CoCu@NC-750 could be attributed to its carbon encapsulation. This suggests that the pseudorhombic dodecahedral shape of CoCu@NC-750 was maintained

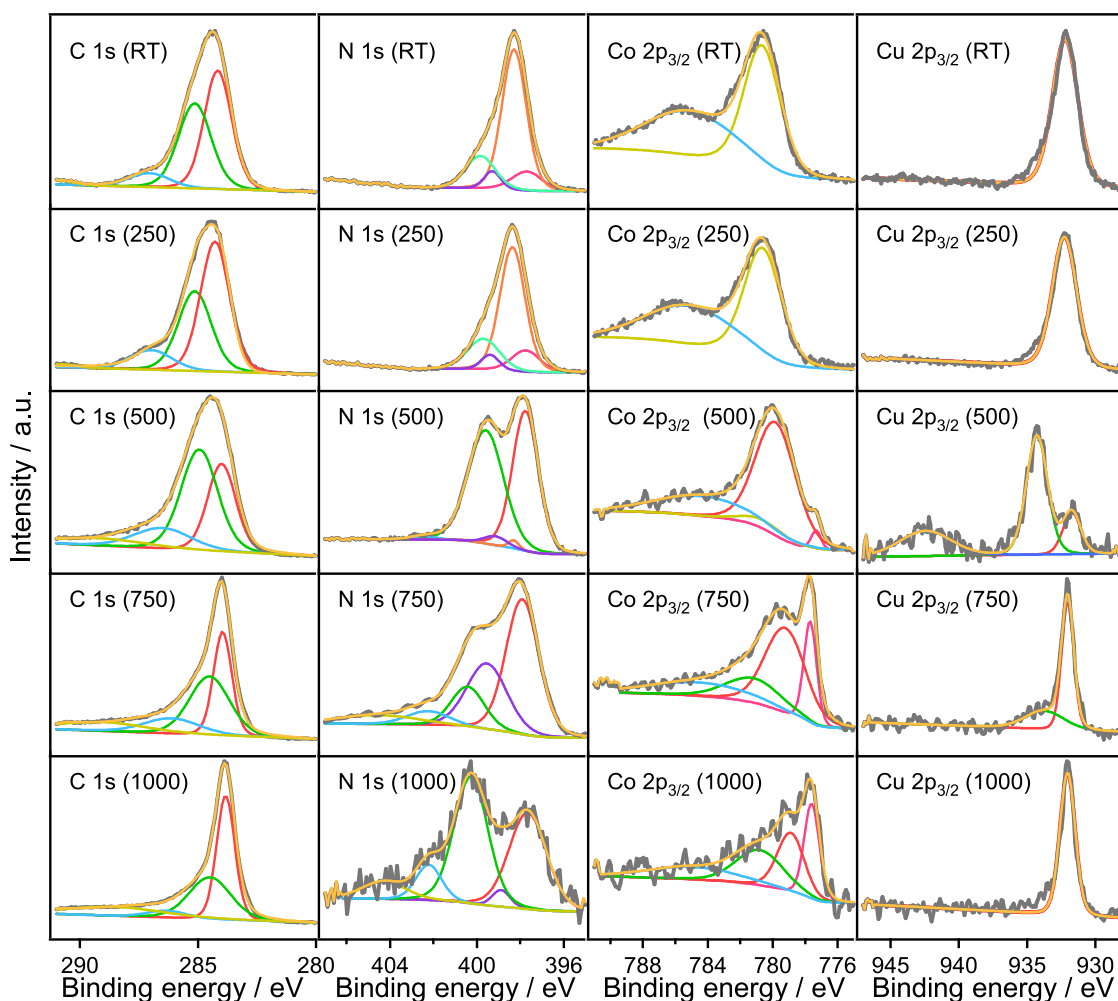


**Figure 6.** Deconvoluted XPS spectra for C 1s, N 1s, Co  $2p_{3/2}$ , and Cu  $2p_{3/2}$  of CoCu-ZIF calcined at different temperatures (RT, 250, 500, 750, and 1000 °C): CoCu-ZIF, CoCu@NC-250, CoCu@NC-500, CoCu@NC-750, and CoCu@NC-1000.

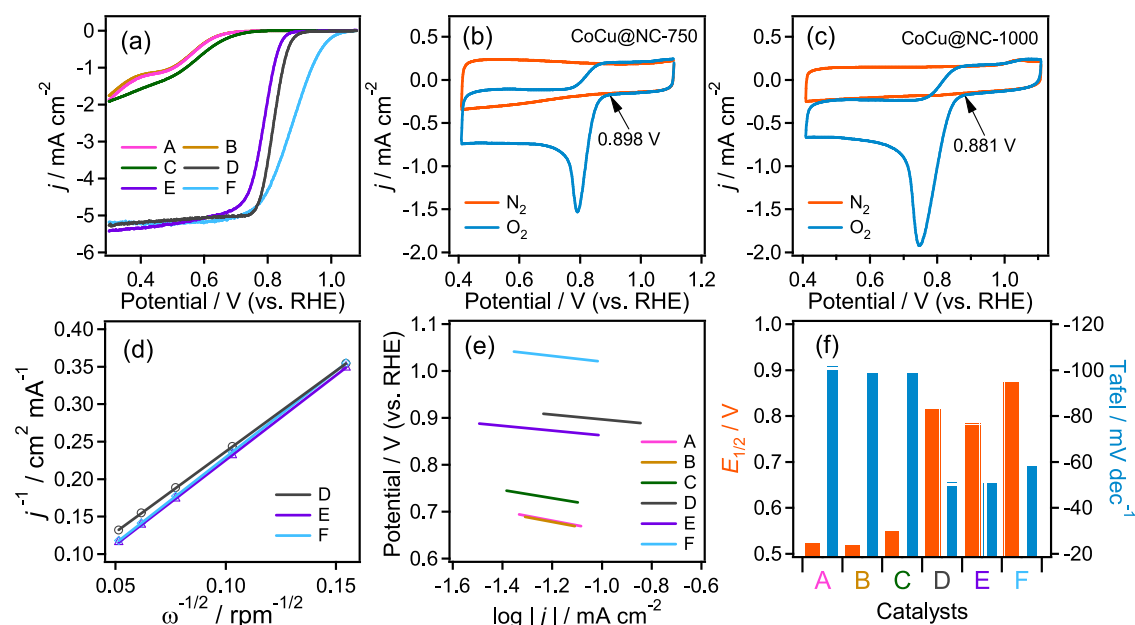
without any distortion even after the pyrolysis of the CoCu-ZIF template.

Figure S5b shows the Raman spectra of the prepared catalysts. The  $690.7\text{ cm}^{-1}$  peak of CoCu-ZIF corresponds to the vibrational mode of the HMIM ligand.<sup>49</sup> CoCu@NC-250 and CoCu-ZIF exhibited the same Raman spectra. In contrast to the typical Raman spectra exhibited by previously reported ZIF-67 structures, the Raman spectrum of CoCu-ZIF showed low peak intensities below  $1000\text{ cm}^{-1}$ . This was attributed to the rapid formation of the ZIF structure at elevated temperatures in the presence of EG rather than under mild synthesis conditions. Moreover, the characteristic D and G bands from carbon allotropes were observed at  $1350.3$  and  $1585.8\text{ cm}^{-1}$ , respectively, in CoCu@NC-500, CoCu@NC-750, and CoCu@NC-1000. The ratios of  $I_D$  to  $I_G$  for CoCu@NC-500, CoCu@NC-750, and CoCu@NC-1000 were 0.810, 0.718, and 0.843, respectively. The lower  $I_D$  to  $I_G$  ratio observed in CoCu@NC-750 was attributed to structural stability during pyrolysis. This can enhance the catalyst activity owing to the increased conductivity of the catalyst structure encapsulated by N-doped carbon.

FT-IR spectroscopy was conducted to investigate the changes in the functional groups associated with the transformation of CoCu-ZIF to CoCu@NC. Figure S5 shows the FT-IR spectra of the modified samples subjected

to various pyrolysis conditions. Both CoCu-ZIF and CoCu@NC-250 exhibited identical spectral patterns consistent with previous physicochemical analyses.<sup>50</sup> These spectra exhibited C–H and N–H stretching vibrations at  $2900\text{--}2950$  and  $2500\text{--}3000\text{ cm}^{-1}$ , respectively.<sup>50</sup> Additionally, stretching vibrations of C–N, C=N, and C=C were observed between  $1300$  and  $1600\text{ cm}^{-1}$ . The distinct FT-IR spectra were not observed for the structures of the carbon-encapsulated CoCu@NC-750 and CoCu@NC-1000. However, in the case of CoCu@NC-500, a weak signal originating from the imidazole functional groups was detected. These results suggest that the optimal pyrolysis conditions contribute to the formation of the shell structure of metal particles within the N-doped carbon, which subsequently influences catalytic activity and stability.

The surface chemical states and elemental compositions of the C, N, Co, and Cu species were further investigated using XPS. Figure 6 shows the C 1s, N 1s, Co  $2p_{3/2}$ , and Cu  $2p_{3/2}$  spectra of the catalysts and their Gaussian-fitted results. The C 1s spectra was fitted into four peaks: the peak at the binding energy (BE) of  $284.2\text{--}284.8\text{ eV}$  is attributed to graphitized  $sp^2\text{-C}$  and  $sp^3\text{-C}$  and those at the higher BEs of  $285.1$  and  $287.1\text{ eV}$  are attributed to C–N and C–O, respectively.<sup>51</sup> As the C content on the catalyst surface increased from 68.4% to 95.6%, the total content of Co (or Cu) decreased from 4.9% (3.0%) to 0.6% (0.5%), as shown in Table S1. The higher  $sp^3\text{-}$



**Figure 7.** ORR electrocatalysis: (A) CoCu-ZIF, (B) CoCu@NC-250, (C) CoCu@NC-500, (D) CoCu@NC-750, (E) CoCu@NC-1000, and (F) Pt/C. (a) LSV curves measured in a 0.1 M KOH solution at a scan rate of  $10 \text{ mV s}^{-1}$  (rotation rate = 1600 rpm). (b, c) CVs obtained in a 0.1 M KOH at a scan rate of  $20 \text{ mV s}^{-1}$  with O<sub>2</sub> or N<sub>2</sub> purging at CoCu@NC-750 and CoCu@NC-1000, respectively. (d) K–L plots. (e) Tafel slopes. (f) Comparison of  $E_{1/2}$  (vs RHE) and Tafel slopes from panels (a) and (e).

C content in CoCu-ZIF was transformed into sp<sup>2</sup>-C in CoCu@NC, where the sp<sup>2</sup>-C/sp<sup>3</sup>-C ratio increased from 0.678 to 3.821 (Table S1).

The N 1s spectra were fitted to four peaks at 397.9, 399.6, 400.4, and 402.2 eV, corresponding to pyridinic N, Co–N, pyrrolic N, and graphitic N, respectively.<sup>52</sup> The pyrolysis of CoCu-ZIF led to an increase in the pyrrolic N and graphitic N contents. CoCu@NC-750 has a higher Co–N content, likely attributable to the optimal pyrolysis temperature facilitating the combination of Co metal with N (Table S2). The Co 2p<sub>3/2</sub> spectra were fitted into either two or four peaks at 777.7, 779.2, 781.2, and 784.5 eV, corresponding to the Co metal, Co–C, Co–N, and the satellite of Co (or possibly CoO), respectively.<sup>53</sup> In contrast, two distinct Cu peaks corresponding to Cu metal or Cu(I) oxide and Cu(II) were observed at 932.1 and 934.2–942.4 eV, respectively.<sup>54</sup> The presence of Cu(II) is likely due to the dissolution of copper ions during the acid wash postpyrolysis. Hence, a pyrolysis temperature of 750 °C was proved to be optimal for preserving the structural integrity of ZIF, enabling N doping, and ensuring a uniform distribution of metal nanoparticles on the carbon matrix.

**ORR Electrocatalysis.** The ORR catalytic activity of a series of CoCu@NC catalysts was investigated in a 0.1 M KOH solution using CV or RRDE techniques. CoCu-ZIF and Pt/C catalysts were also examined for comparison. Figure 7a shows the linear sweep voltammetry (LSV) curves for all the synthesized catalysts. CoCu-ZIF, CoCu@NC-250, and CoCu@NC-500 showed low current densities and half-wave potentials ( $E_{1/2}$ ). In contrast, CoCu@NC-750 and CoCu@NC-1000 exhibited relatively higher  $E_{1/2}$  values of 0.816 and 0.783 V, respectively, compared to the others. The onset potentials exhibited a similar trend to the  $E_{1/2}$  values, indicating the superior ORR activity of CoCu@NC-750. Notably, despite being nonprecious metal catalysts, CoCu@NC-750 and CoCu@NC-1000 showed steeper slopes in the RDE voltammetry curves in the mixed kinetic-diffusion-

controlled region than those of Pt-20/C. This suggests a four-electron transfer mechanism for CoCu@NC-750 and CoCu@NC-1000. The distinction between CoCu@NC-750 and Pt/C becomes even clearer with the variation in rpm in the RDE voltammetry curves (Figure S6). For a more detailed measurement, electrodes incorporating the highly active CoCu@NC-750 and CoCu@NC-1000 catalysts were further evaluated using CVs, confirming results consistent with the onset potentials shown in LSV (Figure 7b,c). The Koutecky–Levich (K–L) plots in Figure 7d show that the electron transfer numbers ( $n$ ) of CoCu@NC-750, CoCu@NC-1000, and Pt/C were 3.79, 3.75, and 3.94, respectively. This demonstrates the superiority of CoCu@NC catalysts in facilitating a near four-electron transfer process, which is pivotal for the efficient oxygen reduction reaction (ORR), closely approaching the ideal performance exhibited by Pt/C. The Tafel slopes revealed that CoCu@NC-750 ( $-50.9 \text{ mV dec}^{-1}$ ) exhibited the lowest slope among all the catalysts (Figure 7e). The lower Tafel slope of CoCu@NC-750 than that of Pt/C ( $-58.1 \text{ mV dec}^{-1}$ ) indicated its enhanced catalytic activity, which is attributed to N doping and structural stability after pyrolysis. Figure 7f showed that CoCu@NC-750 has superior ORR catalytic activity compared to the other synthesized catalysts, particularly in terms of  $E_{1/2}$  and Tafel slopes. Although the  $E_{1/2}$  (0.875 V vs RHE) of the commercial Pt/C catalyst is higher than that of CoCu@NC-750, the unique pseudorhombic dodecahedral core shape of CoCu and its N-doped carbon shell contributed to a steeper RDE curve slope and a lower Tafel slope. The measured electrochemical catalytic activities are listed in Table 1.

**Electrochemical Catalytic Characteristics.** Figure 8a shows the capacitive current density in relation to the scan rate, where the slope provides insight into the active surface area of the catalyst. The capacitances relative to the active surface area for all catalysts were in the following order: CoCu@NC-750 ( $C_{dl} = 10.91 \text{ mF cm}^{-2}$ ) > CoCu@NC-1000

**Table 1. Electrochemical ORR characteristics of the catalysts**

catalysts	$E_{1/2}$ [V]	$E_{\text{onset}}$ [V]	$n$	$\text{HO}_2^-$ [%]	$C_{\text{dl}}$ [ $\text{mF cm}^{-2}$ ]
CoCu@NC-750	0.816	0.896	3.80	9.94	10.91
CoCu@NC-1000	0.783	0.864	3.78	10.65	2.35
Pt/C	0.875	1.017	3.91	4.07	

( $C_{\text{dl}} = 2.35 \text{ mF cm}^{-2}$ ) > CoCu@NC-500 ( $C_{\text{dl}} = 1.39 \text{ mF cm}^{-2}$ ) > CoCu@NC-250 ( $C_{\text{dl}} = 0.59 \text{ mF cm}^{-2}$ )  $\approx$  CoCu-ZIF ( $C_{\text{dl}} = 0.71 \text{ mF cm}^{-2}$ ). This order is consistent with the ORR catalytic activity trend. CoCu@NC-750 exhibited a notably higher slope than the other catalysts, which could be attributed to its well-defined pseudorhombic dodecahedron structure, whereas the other catalysts experienced more extensive structural distortion. The ORR performance of these catalysts is influenced not only by the expanded specific surface area but also by the consistent distribution of the CoCu core within the pseudorhombic dodecahedron framework, which enhances the electrical conductivity and electron transfer rate. The direct transformation of ORR intermediates into the  $\text{OH}^-$  product is significant. Subsequently, the RRDE technique was used to calculate the yield of the peroxide ( $\text{HO}_2^-$ ) intermediates and the  $n$  values of the different catalysts. The  $\text{HO}_2^-$  yields (%) were calculated using the following equation:  $200 \times (I_r/N) / ((I_d + I_r)/N)$ , where  $I_d$  and  $I_r$  represent the ring and the disk in the RRDE (Figure 8b,c) and  $N$  indicates collection efficiency.<sup>55</sup> The order of the  $\text{HO}_2^-$  yields was as follows: CoCu@NC-750 (9.9%) < CoCu@NC-1000 (10.7%) < CoCu@NC-500 (22.1%), which indicates that the  $\text{HO}_2^-$  yields increased as the  $n$  value decreased. This is consistent

with the RDE results, indicating that the ORR of the proposed CoCu@NC-750 nanostructure likely follows a direct four-electron transfer pathway.

Electrochemical impedance spectroscopy (EIS) was used to analyze the kinetics of each catalyst. The charge-transfer resistance values ( $R_{\text{ct}}$ ), estimated from the semicircle at low frequency (high  $Z'$ ), showed that CoCu@NC-750 and CoCu@NC-1000 exhibited lower charge-transfer efficiency than those of the other catalysts (Figure 8d). This was because CoCu@NC-250 and CoCu@NC-500, which were pyrolyzed at comparatively low temperatures, exhibited minimal carbonization. The charge-transfer resistance values for all catalysts were in the order of CoCu-ZIF > CoCu@NC-250 > CoCu@NC-500 > CoCu@NC-1000 ( $Z' = 213.1$ ) > CoCu@NC-750 ( $Z' = 173.2$ ). In addition to its catalytic performance, CoCu@NC-750 demonstrated high stability and durability during the ORR. The overpotential of CoCu@NC-750 at  $E_{1/2}$  shifted positively by 11 mV after 10,000 CV cycles (Figure 8e), which is smaller than that of commercial Pt/C (55 mV). These results suggest that CoCu@NC-750 retained its high catalytic activity and superior stability after long-term cycling during the ORR. Furthermore, during a 12-h ORR process, the current density of CoCu@NC-750 decreased by 0.8%, whereas that of Pt/C showed a larger decline of 8.3% (Figure 8f). These results reveal the enhanced stability of CoCu@NC-750 compared to that of Pt/C, likely due to the N-doped carbon coating on the CoCu-core surface.

The superior catalytic activity of CoCu@NC-750 is attributed to several factors. The bimetallic core enhances electron conductivity and modifies the adsorption energy of the reaction intermediates, thereby limiting their accumulation.

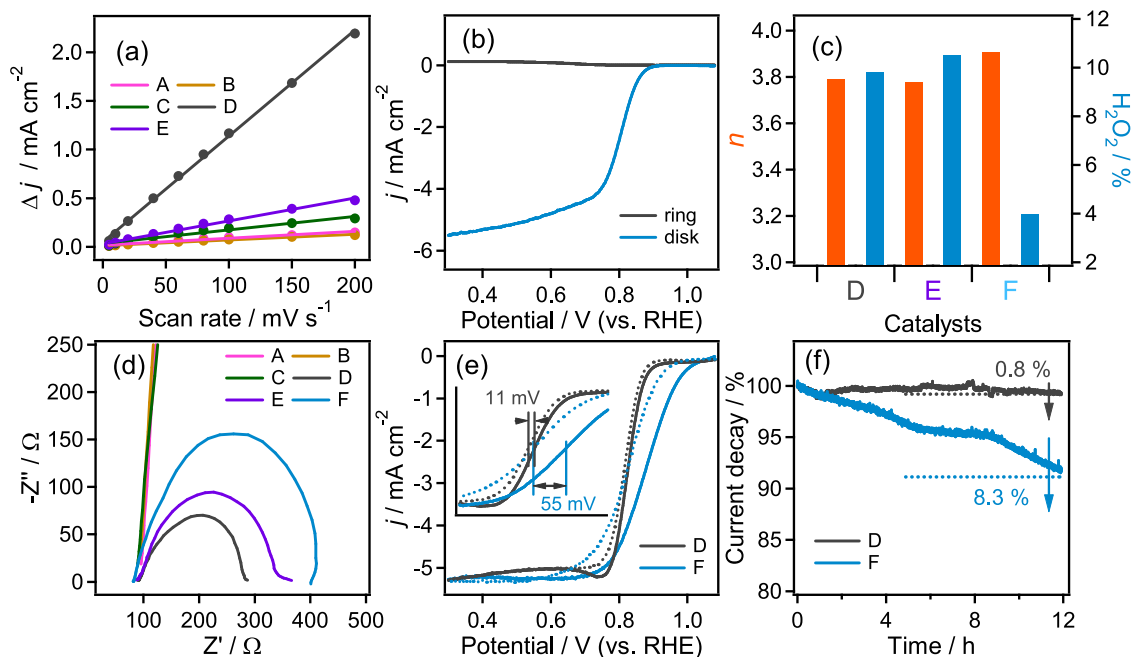


**Figure 8.** Electrochemical catalytic characteristics of (A) CoCu-ZIF, (B) CoCu@NC-250, (C) CoCu@NC-500, (D) CoCu@NC-750, (E) CoCu@NC-1000, and (F) Pt/C. (a) Plots of the capacitive current density ( $\Delta j$  at 0.67 V vs RHE) as a function of the scan rate obtained from cyclic voltammograms (CVs). (b) Representative RRDE voltammograms of CoCu@NC-750 in 0.1 M KOH at a scan rate of  $10 \text{ mV s}^{-1}$  (rotation rate = 1600 rpm). (c)  $n$ -values and peroxide yield at 0.3 V (vs RHE) obtained from (D), (E), and (F). (d) EIS measurements of different catalysts for ORR in an  $\text{O}_2$ -saturated 0.1 M KOH solution at a potential of 0.85 V vs RHE (rotation rate = 1600 rpm). (e) Stability test for (D) and (F) before and after 10,000 cycles of ORR in a 0.1 M KOH solution at a scan rate of  $10 \text{ mV s}^{-1}$  (inset: magnified view of the  $E_{1/2}$  region). (f) Chronoamperometric  $i-t$  responses of (D) and (F) in an  $\text{O}_2$ -saturated 0.1 M KOH solution at 1600 rpm at a potential of 0.71 V (vs RHE) for 12 h. The measured values were converted into current percentages.

The carbon layer shielding the transition metals contributes to improving catalyst stability and durability during the electrode reaction process. The carbon layer enveloping the CoCu surface, influenced by N doping and the partial formation of CNTs, leads to a significant increase in the surface area, thereby enhancing the number of catalytic active sites. These combined effects contributed to the high ORR catalytic activity of the optimized CoCu@NC-750 structure.

## CONCLUSIONS

The CoCu-ZIF(7:3) structure, possessing a well-defined pseudorhombic dodecahedral structure with uniformly distributed Co and Cu, was identified as an optimal precursor for fuel cell cathode catalysts. The presence of hydrazine facilitated the formation of a uniformly shaped structure at high temperatures. Among the synthesized CoCu@NC catalysts, CoCu@NC-750 demonstrated the best results in terms of  $E_{1/2}$ , electron transfer reaction, and Tafel slope in the evaluation of ORR catalytic activity. In stability tests, CoCu@NC-750 exhibited minimal overpotential change after 10,000 CV cycles and only a 0.8% decrease in current density over a 12-h ORR process, outperforming commercial Pt/C. The pseudorhombic dodecahedral framework of the CoCu core and its surrounding carbonaceous layer likely played a role in enhancing both catalytic activity and stability. The RRDE results indicated a low generation rate of the intermediate peroxide, suggesting that the ORR proceeds via a complete four-electron transfer reaction. Overall, CoCu@NC-750 synthesized under optimized conditions demonstrated comparable catalytic activity to that of commercial Pt/C, which indicates its potential as an alternative catalyst to Pt in ORR.

## ASSOCIATED CONTENT

### Supporting Information

The Supporting Information is available free of charge at <https://pubs.acs.org/doi/10.1021/acsomega.4c01667>.

SEM images of synthesized CoCu(7:3)-ZIF, CoFe(7:3)-ZIF, CoMn(7:3)-ZIF, and CoNi(7:3)-ZIF. Photographs of the color changes in  $\text{Co}^{2+}$  and  $\text{Cu}^{2+}$  solutions at each experimental stage. The FT-IR spectra of each catalyst. RDE voltammetry curves for the ORR on CoCu@NC-750 and Pt/C catalysts. Atomic percentages of each catalyst calculated from XPS survey spectral data. (PDF)

## AUTHOR INFORMATION

### Corresponding Author

**Jun Ho Shim** – Department of Chemistry, Daegu University, Gyeongsan 38453, Republic of Korea; Department of Chemistry Education, Daegu University, Gyeongsan 38453, Republic of Korea; [orcid.org/0000-0002-6734-3564](https://orcid.org/0000-0002-6734-3564); Email: [junhoshim@daegu.ac.kr](mailto:junhoshim@daegu.ac.kr)

### Authors

**Sunguk Noh** – Department of Chemistry, Daegu University, Gyeongsan 38453, Republic of Korea; [orcid.org/0000-0002-5055-578X](https://orcid.org/0000-0002-5055-578X)

**Hyejin Oh** – Department of Chemistry, Daegu University, Gyeongsan 38453, Republic of Korea

**Jihyun Kim** – Department of Chemistry, Daegu University, Gyeongsan 38453, Republic of Korea

**Sojin Jung** – Department of Chemistry, Daegu University, Gyeongsan 38453, Republic of Korea

Complete contact information is available at: <https://pubs.acs.org/doi/10.1021/acsomega.4c01667>

## Notes

The authors declare no competing financial interest.

## ACKNOWLEDGMENTS

This work was supported by the National Research Foundation of Korea (NRF) grant funded by the Korean Government (MSIT) (2021R1F1A1063825 and RS-2024-00339411) and by the Technology Development Program (S3259451) funded by the Ministry of SMEs and Startups (MSS) of Korea. This work was also supported by the Korea Sanhak Foundation (KSF) in 2024.

## REFERENCES

- (1) Wu, S.; Salmon, N.; Li, M. M.-J.; Bañares-Alcántara, R.; Tsang, S. C. E. Energy decarbonization via green  $\text{H}_2$  or  $\text{NH}_3$ ? *ACS Energy Lett.* **2022**, *7*, 1021–1033.
- (2) Wang, J.; Kim, D.; Park, J. H.; Ryu, S.; Shokouhimehr, M.; Jang, H. W. Prospects and promises in two-electron water oxidation for hydrogen peroxide generation. *Energy Fuels* **2023**, *37*, 17629–17651.
- (3) Seong, Y.; Kweon, S.; Shim, J. H. Investigation of Stable and Selective Nitrogen Reduction Reaction Using Encapsulated FeMoS<sub>2</sub> Directly Grown on Carbon Cloth. *Energy Fuels* **2023**, *37*, 15967–15975.
- (4) Liu, Z.; Zhao, Z.; Peng, B.; Duan, X.; Huang, Y. Beyond extended surfaces: understanding the oxygen reduction reaction on nanocatalysts. *J. Am. Chem. Soc.* **2020**, *142*, 17812–17827.
- (5) Zhang, Y.; Fu, H.; He, C.; Zhang, H.; Li, Y.; Yang, G.; Cao, Y.; Wang, H.; Peng, F.; Yang, X.; Yu, H. Configuration sensitivity of electrocatalytic oxygen reduction reaction on nitrogen-doped graphene. *J. Phys. Chem. Lett.* **2022**, *13*, 6187–6193.
- (6) Huang, H.; Yu, D.; Hu, F.; Huang, S. C.; Song, J.; Chen, H. Y.; Li, L. L.; Peng, S. Clusters induced electron redistribution to tune oxygen reduction activity of transition metal single-atom for metal–air batteries. *Angew. Chem., Int. Ed.* **2022**, *134*, No. e202116068, DOI: 10.1002/anie.202116068.
- (7) Gong, L.; Zhu, J.; Xia, F.; Zhang, Y.; Shi, W.; Chen, L.; Yu, J.; Wu, J.; Mu, S. Marriage of ultralow platinum and single-atom MnN<sub>4</sub> moiety for augmented ORR and HER catalysis. *ACS Catal.* **2023**, *13*, 4012–4020.
- (8) Liang, L.; Jin, H.; Zhou, H.; Liu, B.; Hu, C.; Chen, D.; Zhu, J.; Wang, Z.; Li, H.-W.; Liu, S.; He, D.; Mu, S. Ultra-small platinum nanoparticles segregated by nickel sites for efficient ORR and HER processes. *J. Energy Chem.* **2022**, *65*, 48–54.
- (9) Jin, H.; Yu, R.; Hu, C.; Ji, P.; Ma, Q.; Liu, B.; He, D.; Mu, S. Size-controlled engineering of cobalt metal catalysts through a coordination effect for oxygen electrocatalysis. *Appl. Catal., B* **2022**, *317*, No. 121766.
- (10) Wang, Z.; Zhou, X.; Jin, H.; Chen, D.; Zhu, J.; Hempelmann, R.; Chen, L.; Mu, S. Ionic liquid-derived FeCo alloys encapsulated in nitrogen-doped carbon framework as advanced bifunctional catalysts for rechargeable Zn-air batteries. *J. Alloys Compd.* **2022**, *908*, No. 164565.
- (11) Wang, Z.; Jin, H.; Meng, T.; Liao, K.; Meng, W.; Yang, J.; He, D.; Xiong, Y.; Mu, S. Fe, Cu-coordinated ZIF-derived carbon framework for efficient oxygen reduction reaction and Zinc–air batteries. *Adv. Funct. Mater.* **2018**, *28*, No. 1802596, DOI: 10.1002/adfm.201802596.
- (12) Gao, J.; Wang, Y.; Wu, H.; Liu, X.; Wang, L.; Yu, Q.; Li, A.; Wang, H.; Song, C.; Gao, Z.; Peng, M.; Zhang, M.; Ma, N.; Wang, J.; Zhou, W.; Wang, G.; Yin, Z.; Ma, D. Construction of a sp<sup>3</sup>/sp<sup>2</sup> carbon interface in 3D N-doped nanocarbons for the oxygen reduction reaction. *Angew. Chem., Int. Ed.* **2019**, *58*, 15089–15097.
- (13) Li, Y.; Wang, X.; Wang, H.; Tan, X.; Liu, D.; Gui, J.; Gao, J.; Yin, Z.; Ma, N.; Wang, Y. Pharaoh's Snakes' reaction-derived carbon

with favorable structure and composition as metal-free oxygen reduction reaction electrocatalyst. *Catalysts* **2023**, *13*, 1059.

(14) Gao, J.; Ma, N.; Zheng, Y.; Zhang, J.; Gui, J.; Guo, C.; An, H.; Tan, X.; Yin, Z.; Ma, D. Cobalt/nitrogen-doped porous carbon nanosheets derived from polymerizable ionic liquids as bifunctional electrocatalyst for oxygen evolution and oxygen reduction reaction. *ChemCatChem* **2017**, *9*, 1601–1609.

(15) Lv, J. Q.; Lang, Z. L.; Fu, J. Q.; Lan, Q.; Liu, R.; Zang, H. Y.; Li, Y. G.; Ye, D. D.; Streb, C. Molecular iron oxide clusters boost the oxygen reduction reaction of platinum electrocatalysts at near-neutral pH. *Angew. Chem.* **2022**, *134*, No. e202202650.

(16) Zhou, X.; Wu, M.; Chen, K.; Ci, S.; Wen, Z. Metal–organic framework-loaded carbon-encapsulated nano-catalyst as a pH-universal oxygen reduction reaction electrocatalyst for various fuel cell devices. *Catal. Sci. Technol.* **2023**, *13*, 3009–3019.

(17) Nguyen, A. T. N.; Shim, J. H. All carbon hybrid N-doped carbon dots/carbon nanotube structures as an efficient catalyst for the oxygen reduction reaction. *RSC Adv.* **2021**, *11*, 12520–12530.

(18) Chaturvedi, A.; Kundu, P. P. Enhancing sustainable bioelectricity generation using facile synthesis of nanostructures of bimetallic Co–Ni at the combined support of halloysite nanotubes and reduced graphene oxide as novel oxygen reduction reaction electrocatalyst in single-chambered microbial fuel cells. *Int. J. Hydrogen Energy* **2022**, *47*, 29413–29429.

(19) Pumera, M. Graphene-based nanomaterials and their electrochemistry. *Chem. Soc. Rev.* **2010**, *39*, 4146–4157.

(20) Yang, Q.; Xiao, Z.; Kong, D.; Zhang, T.; Duan, X.; Zhou, S.; Niu, Y.; Shen, Y.; Sun, H.; Wang, S.; Zhi, L. New insight to the role of edges and heteroatoms in nanocarbons for oxygen reduction reaction. *Nano Energy* **2019**, *66*, No. 104096.

(21) Xue, J.; Deng, S.; Wang, R.; Li, Y. Efficient synergistic effect of trimetallic organic frameworks derived as bifunctional catalysis for the rechargeable zinc-air flow battery. *Carbon* **2023**, *205*, 422–434.

(22) Beyeon, A.; Yun, W. C.; Kim, J. M.; Lee, J. W. Non-precious metal catalysts for two-electron oxygen reduction reaction. *ChemElectroChem* **2023**, *10*, No. e202300234.

(23) Flores-Lasluisa, J. X.; Huerta, F.; Cazorla-Amorós, D.; Morallón, E. Transition metal oxides with perovskite and spinel structures for electrochemical energy production applications. *Environ. Res.* **2022**, *214*, No. 113731.

(24) Ren, Q.; Wang, H.; Lu, X. F.; Tong, Y. X.; Li, G. R. Recent progress on MOF-derived heteroatom-doped carbon-based electrocatalysts for oxygen reduction reaction. *Adv. Sci.* **2018**, *5*, No. 1700515.

(25) Tong, J.; Li, W.; Bo, L.; Ma, J.; Li, T.; Li, Y.; Zhang, Q.; Fan, H. Composite of hierarchically porous N-doped carbon/carbon nanotube with greatly improved catalytic performance for oxygen reduction reaction. *ACS Sustainable Chem. Eng.* **2018**, *6*, 8383–8391.

(26) Wang, L.; Xu, M.; Li, H.; Huang, Z.; Wang, L.; Taylor Isimjan, T.; Yang, X. Mn-doped Zn metal–organic framework-derived porous N-doped carbon composite as a high-performance nonprecious electrocatalyst for oxygen reduction and aqueous/flexible zinc–air batteries. *Inorg. Chem.* **2023**, *62*, 13284–13292.

(27) Lai, Q.; Zhu, J.; Zhao, Y.; Liang, Y.; He, J.; Chen, J. MOF-based metal-doping-induced synthesis of hierarchical porous Cu–N/C oxygen reduction electrocatalysts for Zn–air batteries. *Small* **2017**, *13*, No. 1700740.

(28) Douka, A. I.; Xu, Y.; Yang, H.; Zaman, S.; Yan, Y.; Liu, H.; Salam, M. A.; Xia, B. Y. A zeolitic-imidazole frameworks-derived interconnected macroporous carbon matrix for efficient oxygen electrocatalysis in rechargeable zinc–air batteries. *Adv. Mater.* **2020**, *32*, No. 2002170.

(29) Niu, W.-J.; Sun, Q.-Q.; He, J.-Z.; Chen, J.-L.; Gu, B.; Liu, M.-J.; Chung, C.-C.; Wu, Y.; Chueh, Y.-L. Zeolitic imidazolate framework-derived copper single atom anchored on nitrogen-doped porous carbon as a highly efficient electrocatalyst for the oxygen reduction reaction toward Zn–air battery. *Chem. Mater.* **2022**, *34*, 4104–4114.

(30) Jadhav, H. S.; Bandal, H. A.; Ramakrishna, S.; Kim, H. Critical review, recent updates on zeolitic imidazolate framework-67 (ZIF-67)

and its derivatives for electrochemical water splitting. *Adv. Mater.* **2022**, *34*, No. 2107072.

(31) Li, X.; Liang, H.; Liu, X.; Zhang, Y.; Liu, Z.; Fan, H. Zeolite imidazolate frameworks (ZIFs) derived nanomaterials and their hybrids for advanced secondary batteries and electrocatalysis. *Chem. Rec.* **2022**, *22*, No. e202200105.

(32) Kaushik, S.; Chand, P.; Sharma, S. Asymmetric supercapacitor device fabrication of pristine Zeolitic Imidazolate Framework-67 with ultrahigh performance and cyclic stability. *J. Energy Storage* **2024**, *78*, No. 110033.

(33) Al Murisi, M.; Al-Asheh, S.; Abdelkareem, M. A.; Aidan, A.; Elsaid, K.; Olabi, A. G. In situ growth of zeolite imidazole frameworks (ZIF-67) on carbon cloth for the application of oxygen reduction reactions and microbial fuel cells. *ACS Omega* **2023**, *8*, 44514–44522.

(34) Yan, T.-X.; Li, X.-J.; Chen, L.; Zhang, Z.-H.; Chen, Q.; He, M.-Y. Efficient adsorption separation of xylene isomers in zeolitic imidazolate framework-67@MCF hybrid materials. *J. Solid State Chem.* **2022**, *307*, No. 122819.

(35) Khan, S.; Noor, T.; Iqbal, N.; Pervaiz, E.; Yaqoob, L. A zeolitic imidazolate framework (ZIF-67) and graphitic carbon nitride (g-C<sub>3</sub>N<sub>4</sub>) composite based efficient electrocatalyst for overall water-splitting reaction. *RSC Adv.* **2023**, *13*, 24973–24987.

(36) Shan, Y.; Zhang, M.; Bai, Y.; Du, M.; Guo, X.; Pang, H. Design and synthesis of transition metal oxide/zeolitic imidazolate framework-67 composites. *Chem. Eng. J.* **2022**, *429*, No. 132146.

(37) Nørskov, J. K.; Rossmeisl, J.; Logadottir, A.; Lindqvist, L.; Kitchin, J. R.; Bligaard, T.; Jonsson, H. Origin of the overpotential for oxygen reduction at a fuel-cell cathode. *J. Phys. Chem. B* **2004**, *108*, 17886–17892.

(38) Kuang, M.; Wang, Q.; Han, P.; Zheng, G. Cu, Co-embedded N-enriched mesoporous carbon for efficient oxygen reduction and hydrogen evolution reactions. *Adv. Energy Mater.* **2017**, *7*, No. 1700193.

(39) Yu, H.; Fisher, A.; Cheng, D.; Cao, D. Cu, N-codoped hierarchical porous carbons as electrocatalysts for oxygen reduction reaction. *ACS Appl. Mater. Interfaces* **2016**, *8*, 21431–21439.

(40) Wang, J.; Wang, K.; Wang, F.-B.; Xia, X.-H. Bioinspired copper catalyst effective for both reduction and evolution of oxygen. *Nat. Commun.* **2014**, *5*, No. 5285.

(41) Noh, S.; Shim, J. H. Hollow Nickel Nanochains Coated with Nickel-Iron Hydroxide for Oxygen Evolution. *ACS Appl. Nano Mater.* **2023**, *6*, 15887–15895.

(42) Guo, L.; Liang, F.; Wen, X.; Yang, S.; He, L.; Zheng, W.; Chen, C.; Zhong, Q. Uniform magnetic chains of hollow cobalt mesospheres from one-pot synthesis and their assembly in solution. *Adv. Funct. Mater.* **2007**, *17*, 425–430.

(43) Krekeler, T.; Straßer, A. V.; Graf, M.; Wang, K.; Hartig, C.; Ritter, M.; Weissmüller, J. Silver-rich clusters in nanoporous gold. *Mater. Res. Lett.* **2017**, *5*, 314–321.

(44) Asadi, F.; Azizi, S. N.; Ghasemi, S. A novel non-precious catalyst containing transition metal in nanoporous cobalt based metal-organic framework (ZIF-67) for electrooxidation of methanol. *J. Electroanal. Chem.* **2019**, *847*, No. 113181.

(45) Davoodian, N.; Nakhaei Pour, A.; Izadyar, M.; Mohammadi, A.; Salimi, A.; Kamali Shahri, S. M. Fischer–Tropsch synthesis using zeolitic imidazolate framework (ZIF-7 and ZIF-8)-supported cobalt catalysts. *Appl. Organomet. Chem.* **2020**, *34*, No. e5747.

(46) Li, J.; Papadopoulos, C.; Xu, J.; Moskovits, M. Highly-ordered carbon nanotube arrays for electronics applications. *Appl. Phys. Lett.* **1999**, *75*, 367–369.

(47) Rodríguez-Manzo, J. A.; Janowska, I.; Pham-Huu, C.; Tolvanen, A.; Krasheninnikov, A. V.; Nordlund, K.; Banhart, F. Growth of single-walled carbon nanotubes from sharp metal tips. *Small* **2009**, *5*, 2710–2715.

(48) Lu, Y.; Pan, H.; Lai, J.; Xia, Y.; Chen, L.; Liang, R.; Yan, G.; Huang, R. Bimetallic CoCu-ZIF material for efficient visible light photocatalytic fuel denitrification. *RSC Adv.* **2022**, *12*, 12702–12709.

(49) Manjunatha, M.; Reddy, G. S.; Mallikarjunaiah, K.; Damle, R.; Ramesh, K. Determination of phase composition of cobalt nano-

particles using  $^{59}\text{Co}$  internal field nuclear magnetic resonance. *J. Supercond. Nov. Magn.* **2019**, *32*, 3201–3209.

(50) Mohsen, M.; Baraka, A.; Naeem, I.; Tantawy, H.; Awaad, M.; Abuzalat, O. Effect of sulfur doping of zinc-imidazole coordination polymer (ZnIm CP) as a novel photocatalyst for degradation of ionic dyes. *BMC Chem.* **2022**, *16*, 86.

(51) Wang, X.; Li, Y. Nanoporous carbons derived from MOFs as metal-free catalysts for selective aerobic oxidations. *J. Mater. Chem. A* **2016**, *4*, 5247–5257.

(52) Miao, Z.; Liu, W.; Zhao, Y.; Wang, F.; Meng, J.; Liang, M.; Wu, X.; Zhao, J.; Zhuo, S.; Zhou, J. Zn-Modified Co@N–C composites with adjusted Co particle size as catalysts for the efficient electroreduction of  $\text{CO}_2$ . *Catal. Sci. Technol.* **2020**, *10*, 967–977.

(53) Guo, C.; Li, Y.; Liao, W.; Liu, Y.; Li, Z.; Sun, L.; Chen, C.; Zhang, J.; Si, Y.; Li, L. Correction: Boosting the oxygen reduction activity of a three-dimensional network Co–N–C electrocatalyst via space-confined control of nitrogen-doping efficiency and the molecular-level coordination effect. *J. Mater. Chem. A* **2018**, *6*, 23906.

(54) Biesinger, M. C. Advanced analysis of copper X-ray photoelectron spectra. *Surf. Interface Anal.* **2017**, *49*, 1325–1334.

(55) Kim, J.; Noh, S.; Shim, J. H. Nitrogen-doped carbon dot/activated carbon nanotube-supported copper nanoparticles as an efficient electrocatalyst for the oxygen reduction reaction. *J. Electroanal. Chem.* **2023**, *937*, No. 117423.